GMR
The Original

NANO - ENABLED COMPUTATIONAL INSIGHTS INTO FRUIT PHYTOCHEMICALS AS DUAL MODULATORS OF INSULIN RECEPTOR AND PPAR

Priya Modhugur Sathyanarayanan[1], Magesh Mohan[1]*, Pavithra Bharathy[2], Swathi T[1], Jaisri J. R[1], Akshaya Varshini S[1], Nashwa S[1]

[1]Department of Pharmaceutical Chemistry, Saveetha College of Pharmacy, Saveetha Institute of Medical and Technical Sciences (SIMATS), Thandalam, Chennai, Tamil Nadu, India - 602105.
[2]Department of Pharmaceutics, Saveetha College of Pharmacy, Saveetha Institute of Medical and Technical Sciences (SIMATS), Thandalam, Chennai, Tamil Nadu, India - 602105
*Corresponding Author
E-mail: mageshm.scop@saveetha.com, priyamodhugur15@gmail.com

ABSTRACT
The rising global burden of type 2 diabetes mellitus underscores the need for therapeutic approaches capable of regulating multiple control points within insulin signalling networks. Although dietary phytochemicals have been widely associated with antidiabetic effects, their practical application is frequently limited by poor molecular stability and variable interaction with biological targets. In this study, a nano-enabled computational strategy was applied to investigate fruit-derived phytochemicals against two complementary antidiabetic targets: a computationally defined organic binding region within the insulin receptor ectodomain (PDB ID: 7BW8), which plays a key role in signal initiation, and peroxisome proliferator-activated receptor gamma (PPARγ; PDB ID: 7AWC), a major regulator of insulin sensitivity. A total of sixty-five phytochemicals identified from banana, mango, and jackfruit were screened using molecular docking and MM-GBSA binding free energy calculations, followed by adsorption and electronic interaction analyses on $AgNO_3$ surfaces to evaluate nano-interface stabilization. Selected high-affinity ligands were further examined through independent 100 ns molecular dynamics simulations using the Desmond engine. Among the screened compounds, 1,3,6-tri-O-galloyl-β-D-glucose displayed strong affinity toward PPARγ, achieving docking scores of approximately −10.4 kcal/mol and MM-GBSA binding energies below −65 kcal/mol, surpassing the reference drug acarbose. In the case of the insulin receptor target, 4-epicyclomusalenone showed stable binding characterized by persistent hydrogen bonds with Asn541 and Ser540, together with sustained hydrophobic interactions involving Trp493 and Tyr492, maintaining an average of three to four contacts throughout the simulation period. Collectively, these findings highlight nano-stabilized phytochemicals as promising dual modulators of insulin signalling pathways and provide a robust computational basis for future experimental validation.

Keywords Nano-enabled drug design, Insulin receptor (7BW8) PPARγ (7AWC), Phytochemical modulation, Molecular dynamics simulation.

INTRODUCTION

Diabetes mellitus is a chronic metabolic disorder characterized by sustained hyperglycaemia arising from impaired insulin secretion, diminished insulin sensitivity, or disruption of glucose regulatory mechanisms (Williams et al., 2014; The Lancet, 2023; Hossain et al., 2024). The global incidence of type 2 diabetes mellitus continues to rise at an alarming rate, imposing a substantial burden on healthcare systems due to its association with long-term complications such as cardiovascular disease, neuropathy, nephropathy, and metabolic dysfunction. Although existing pharmacological interventions are effective in reducing blood glucose levels, prolonged treatment is frequently accompanied by adverse effects, declining therapeutic response, and challenges related to patient adherence. These limitations underscore the need for alternative or complementary therapeutic strategies that offer durable metabolic control with improved safety and tolerability (Rossi et al., 2019).

Dietary plants and edible fruits represent an important source of bioactive compounds with the potential to modulate metabolic pathways relevant to diabetes management. Tropical fruits, including Virupakshi banana (Musa paradisiaca, AAB group), Bangalora mango (Mangifera indica L.), and jackfruit (Artocarpus heterophyllus Lam., cultivar Vellipala), are widely consumed and commonly recommended in nutritional interventions aimed at metabolic

disorders (Antar et al., 2023). These fruits contain diverse classes of phytochemicals such as flavonoids, phenolic acids, glycosides, sterols, and terpenoids, many of which have been associated with antioxidant, anti-inflammatory, and glucose-regulatory effects. Despite promising biological activity, the clinical translation of fruit-derived phytochemicals remains limited by poor aqueous solubility, metabolic instability, low bioavailability, and inconsistent interaction with molecular targets involved in insulin signalling (Poznyak et al., 2020).

Recent advances in green nanotechnology have opened new avenues for enhancing the therapeutic potential of phytochemicals. Silver nanoparticles synthesized using plant-derived compounds as reducing and stabilizing agents have attracted particular interest due to their high surface-area-to-volume ratio and adaptable surface chemistry. In such nano-enabled systems, phytochemicals not only facilitate nanoparticle formation but may also remain associated with the nanoparticle surface, creating hybrid phytochemical–nanometal assemblies (Parvin et al., 2025; Kumar et al., 2023; Simon et al., 2018). This association has the potential to improve ligand stability, optimize molecular orientation, and strengthen noncovalent interactions with biological macromolecules. However, silver-based nanomaterials also pose challenges, including size-dependent cytotoxicity, oxidative stress induction, and variability in biological response, highlighting the importance of mechanistic investigations at the molecular level prior to therapeutic consideration (Omer et al., 2022; Momozawa et al., 2011; Imran et al., 2020).

At the molecular scale, diabetes progression is governed by dysregulation of signalling proteins and transcriptional regulators that coordinate insulin sensitivity, glucose uptake, and inflammatory responses (Sayago-Ayerdi et al., 2021). Peroxisome proliferator-activated receptor gamma (PPARγ) is a key nuclear receptor that regulates adipocyte differentiation, lipid metabolism, and insulin responsiveness. The ligand-binding domain represented by PDB ID: 7AWC undergoes conformational rearrangement upon ligand binding, enabling heterodimerization with the retinoid X receptor and activation of gene expression programs that enhance insulin sensitivity (Sayago-Ayerdi et al., 2021; Willems et al., 2021). While full agonists of PPARγ improve glycaemic control, their clinical use is often limited by adverse metabolic effects, motivating interest in partial agonists or modulators - particularly those derived from natural sources - that fine-tune receptor activity without excessive activation.

Complementing transcriptional regulation, insulin signal initiation is governed by structural and dynamic features of the insulin receptor binding region, represented by PDB ID: 7BW8. Insulin binding to this region is a prerequisite for receptor activation and downstream signalling through pathways such as PI3K/Akt and MAPK, which regulate glucose transport, glycogen synthesis, and lipid metabolism. Disruption of insulin–receptor interactions, whether through oxidative stress, inflammation, or conformational instability, directly contributes to insulin resistance. Stabilization or modulation of this binding interface therefore represents a complementary therapeutic strategy aimed at restoring insulin responsiveness at the receptor level. Together, PPARγ and the insulin binding region represent mechanistically distinct yet interconnected targets that collectively govern both immediate and long-term aspects of insulin signalling. Despite extensive literature describing the antidiabetic potential of phytochemicals and the growing interest in green-synthesized silver nanoparticles, existing studies predominantly examine these components independently. Computational investigations frequently focus on single molecular targets or evaluate free phytochemicals without accounting for nano-interface stabilization effects. Consequently, there remains a clear gap in understanding how nano-associated phytochemicals may simultaneously influence insulin signal initiation and transcriptional regulation of insulin sensitivity. Moreover, the molecular mechanisms through which silver-based nano-interfaces affect ligand stability, binding persistence, and electronic complementarity at diabetes-relevant protein targets remain insufficiently explored. To address these gaps, the present study employs an integrated nano-assisted computational framework to investigate fruit-derived phytochemicals targeting both the insulin binding region (PDB ID: 7BW8) and PPARγ (PDB ID: 7AWC) (Yu et al., 2021).

Molecular docking, binding free energy calculations, nano-interface interaction analysis, and molecular dynamics simulations are combined to elucidate binding behaviour, stability, and dynamic persistence under simulated physiological conditions. While experimental validation lies beyond the scope of this work, the findings provide mechanistic insight into dual-target nano-enabled modulation of insulin signalling pathways and establish a rational foundation for future in vitro and in vivo investigations.

MATERIALS AND METHODS

Selection of Plant Sources and Phytochemical Dataset

Virupakshi banana (Musa paradisiaca, AAB genomic group), Bangalora mango (Mangifera indica L.), and jackfruit (Artocarpus heterophyllus Lam., cultivar Vellipala) were selected based on their traditional dietary relevance and reported benefits in metabolic disorders. Phytochemical constituents reported from the edible pulp of these fruits were compiled through an extensive survey of peer-reviewed literature and phytochemical databases IMMPAT

https://cb.imsc.res.in/imppat Chemical structures of the selected phytochemicals were constructed using ChemDraw and subsequently converted into SMILES format (Mohanraj et al., 2018). Three-dimensional geometries were generated and energetically optimized prior to computational studies to ensure structural accuracy.

Molecular Structure Preparation

A total of sixty-five (65) phytochemical constituents were selected from the edible pulp of Virupakshi banana (Musa paradisiaca, AAB genomic group), Bangalora mango (Mangifera indica L.), and jackfruit (Artocarpus heterophyllus Lam.) based on their reported occurrence in these fruits and document Two-dimensional chemical structures of all 65 phytochemicals were constructed using ChemDraw software (Tran et al., 2020).

The structures were converted into SMILES notation and subsequently transformed into three-dimensional geometries. Prior to interaction analysis, all molecules were energetically optimized to remove steric strain and obtain stable conformations suitable for computational evaluation.

Blender-Based Interaction Analysis

A Blender-based interaction analysis was conducted using a multiscale computational framework that combines quantum mechanical calculations with classical molecular simulations to evaluate phytochemical–nano-interface interactions. Initially, all phytochemical structures were geometrically optimized at the quantum level using density functional theory (DFT) with the B3LYP exchange–correlation functional and the 6-31G basis set to obtain energetically stable conformations. Partial atomic charges were subsequently derived through the restrained electrostatic potential (RESP) approach to ensure consistency between quantum-level calculations and molecular mechanics simulations. Following quantum optimization, the systems were transferred to a classical molecular mechanic's environment. Phytochemical molecules were parameterized using the General Amber Force Field (GAFF), whereas interactions involving the metallic surface were described using parameters derived from the Universal Force Field (UFF).

Energy minimization was performed in two sequential stages, consisting of 5000 steps of steepest descent followed by conjugate gradient minimization, in order to remove steric clashes and unfavourable interactions. The systems were then equilibrated under constant pressure and temperature conditions (NPT ensemble) at 298 K using molecular dynamics simulations for a duration of 1 ns (Ma et al., 2023). After achieving thermal equilibration, adsorption behaviour and interaction energetics were systematically evaluated.

Adsorption strength and surface affinity were quantified by calculating the gradient of adsorption energy with respect to the number of interacting surface atoms (dE_ad/dN_i), providing insight into stability trends across different phytochemicals.

Binding free energies were further estimated using the molecular mechanics–Poisson–Boltzmann surface area (MM-PBSA) approach. In addition, electronic descriptors, including electronegativity (χ), mixing energy (E_mix), and average screen–screen interaction energy (E_ss), were analysed to characterise charge redistribution and electronic contributions at the phytochemical–nano-interface.

Adsorption Locator Studies

The adsorption characteristics of all sixty-five phytochemicals were examined using the Adsorption Locator module implemented in the Materials Studio suite. The metallic surface model was prepared by cleaving the bulk crystal along selected crystallographic orientations, followed by construction of a supercell with sufficient vacuum spacing to minimise periodic boundary effects. Interatomic interactions within the system were modelled using the COMPASS III force field. Sampling of adsorption configurations was carried out using the Metropolis Monte Carlo algorithm, which allows systematic exploration of the adsorption landscape through random translations, rotations, and conformational adjustments of the phytochemical molecules (Kwokal et al., 2013).

Each simulation was performed at 298 K and comprised 50,000 Monte Carlo steps to ensure adequate coverage of low-energy adsorption states. Adsorption energies were computed as the difference between the total energy of the surface–ligand complex and the combined energies of the isolated surface and the free phytochemical.

The analysis enabled identification of energetically preferred adsorption sites, including top, bridge, and hollow positions, as well as estimation of rigid adsorption and deformation energy components. For selected low-energy adsorption complexes, further electronic structure refinement was performed using $Dmol^3$ calculations to improve the accuracy of interaction descriptions.

The resulting adsorption energy gradients (dE_ad/dN_i) for all phytochemicals were subsequently used as a comparative parameter to assess adsorption efficiency and surface interaction behaviour among compounds derived from mango, banana, and jackfruit.

Target Selection and Protein Preparation

The molecular targets selected for the present study were Peroxisome proliferator-activated receptor gamma (PPARG) and the human insulin receptor, roles in insulin sensitivity, glucose uptake, and metabolic regulation. PPARG was represented by its crystal structure in complex with rosiglitazone (PDB ID: 7AWC), The insulin receptor was represented by the cryo-electron microscopy structure of the full-length human insulin receptor ectodomain in complex with one insulin molecule (PDB ID: 7BW8), which preserves the native insulin-binding architecture and receptor flexibility under near-physiological conditions (Sayago-Ayerdi et al., 2021; Willems et al., 2021; Yu et al., 2021; Mohanraj et al., 2018). These structures were chosen to ensure biological relevance, structural completeness, and reliability for nanoparticle–drug interaction studies. Protein structures were prepared using the Protein Preparation Wizard available in the Schrödinger Suite.

The crystallographic coordinates of the selected targets, PPARγ (PDB ID: 7AWC) and the insulin receptor binding region (PDB ID: 7BW8), were imported into Maestro and carefully examined for structural completeness, including missing residues, truncated side chains, and other inconsistencies. Non-essential heteroatoms, buffer components, and crystallographic artefacts were removed, while biologically relevant ligands and cofactors were preserved to maintain structural integrity. Hydrogen atoms were added in accordance with standard valence conventions, and bond orders were assigned appropriately. Protonation states of ionizable residues were optimized at physiological pH using the Epik module to obtain a realistic charge distribution.

Hydrogen-bonding networks were subsequently refined by reorienting hydroxyl groups, amide side chains, and histidine residues to achieve energetically favourable interactions. Water molecules located outside the binding or active regions were removed, whereas conserved water molecules contributing to ligand stabilization were retained where relevant. The prepared protein structures were then subjected to restrained energy minimization using the OPLS4 force field. During this process, hydrogen atoms and flexible side chains were allowed to relax, while the protein backbone was constrained to remain within a predefined root mean square deviation threshold to preserve the experimentally determined conformation (Vianello et al., 2016).

Ligand preparation

Preparation of the sixty-five phytochemical ligands was performed using the LigPrep module of the Schrödinger Suite to obtain chemically consistent and energetically optimized structures for subsequent computational analyses (Mehmood et al., 2025). All ligand geometries were refined using the OPLS4 force field, allowing reliable representation of intramolecular interactions and conformational energetics. Protonation and ionization states were assigned using the Epik program, which generates physiologically relevant charge states within a pH range of 7.0 ± 2.0.

Salt forms and counter-ions were removed to eliminate potential non-specific interactions during docking calculations. Tautomer generation was not included in order to avoid unnecessary expansion of the ligand library and to maintain a consistent comparison across compounds. For molecules containing undefined or flexible stereo genic centers, all chemically plausible stereoisomers were generated, after which a single lowest-energy conformer was retained for each ligand to balance structural relevance with computational efficiency (Ahamed et al., 2024).

Receptor Binding-Site Identification and Grid Generation

Receptor preparation and docking grid generation were performed using the Schrödinger Suite to define appropriate docking environments for the target proteins PPARγ (PDB ID: 7AWC) and the insulin receptor binding region (PDB ID: 7BW8). For the PPARγ structure (7AWC), the docking grid was centered on the experimentally resolved ligand-binding pocket. The co-crystallized ligand was identified and removed prior to grid construction to allow accurate representation of the native binding cavity. Grid generation was conducted using default van der Waals radius scaling parameters (scaling factor of 1.0) with a partial charge cutoff of 0.25, enabling balanced treatment of steric and electrostatic interactions while preserving the geometry of the binding site. In contrast, for the insulin receptor structure (7BW8), no predefined ligand-binding region was available. Therefore, potential binding sites were first identified using the SiteMap module (Mohammed Zaidh et al., 2023). SiteMap analysis was carried out to predict and rank putative binding pockets based on site enclosure, hydrophobic and hydrophilic character, hydrogen-bonding potential, and site point density. A minimum threshold of 15 site points per site was applied, and up to five candidate binding regions were reported. Large cavities were further subdivided to improve spatial resolution, while shallow or surface-exposed regions were excluded to prioritise druggable pockets.

The highest-ranked binding site identified by SiteMap was subsequently selected for grid generation. Docking grids for both protein targets were generated using the standard Glide grid generation protocol, ensuring consistent spatial definition of receptor environments for subsequent molecular docking and interaction analyses.

Molecular Docking

Structure-based molecular docking was conducted using the Glide module within the Schrödinger Suite to evaluate the binding orientations and interaction profiles of the prepared phytochemical ligands within the predefined receptor binding sites. The previously generated receptor grids were treated as rigid docking environments, while all ligands were docked in their energy-minimized conformations and physiologically relevant ionization states. Docking calculations were performed using the extra-precision (XP) mode to enhance discrimination between high- and low-affinity binding poses. Full ligand flexibility was enabled during docking, allowing comprehensive sampling of conformational degrees of freedom, including ring puckering and nitrogen inversion, to ensure thorough exploration of accessible binding configurations. Nonpolar interactions were treated by scaling the van der Waals radii of ligand atoms with low partial charges using a scaling factor of 0.80 and a charge cutoff of 0.15, allowing improved accommodation of ligands within the binding pocket during initial pose generation. Torsional sampling was applied to all predefined functional groups, and Epik-derived protonation state penalties were incorporated into the docking score to account for ionization energetics. Post-docking energy minimization was applied to refine ligand–receptor complexes, with the lowest-energy pose retained for each ligand based on Glide Score ranking (Irfan et al., 2023). The final docked complexes were saved in pose viewer format for subsequent interaction analysis and binding energy evaluation.

MD Simulation

Molecular dynamics (MD) simulations were independently carried out for the standard drug and the top-ranked phytochemical–protein complexes to comparatively assess their dynamic stability and binding behaviour with the target proteins 7AWC and 7BW8.

All simulations were performed using the Desmond module of the Schrödinger Suite under identical computational conditions to ensure consistency. Each protein–ligand complex was solvated using the SPC water model within an orthorhombic periodic boundary box, maintaining a minimum buffer distance of 10 Å from the protein surface. System neutrality was achieved by adding appropriate counterions, and a physiological salt concentration of 0.15 M NaCl was maintained (Priya et al., 2024). The OPLS4 force field was applied to describe both protein and ligand interactions accurately. Before initiating production simulations, all systems were subjected to energy minimization followed by stepwise equilibration using the standard relaxation protocol implemented in Desmond. Temperature equilibration was first performed under constant volume conditions (NVT ensemble), after which pressure equilibration was carried out under constant pressure conditions (NPT ensemble) at 300 K and 1 bar. Temperature and pressure were regulated using the Nosé–Hoover thermostat and the Martyna–Tobias–Klein barostat, respectively. Long-range electrostatic interactions were treated using the particle mesh Ewald approach, and all bonds involving hydrogen atoms were constrained to permit an integration time step of 2 fs Following equilibration, independent production molecular dynamics simulations of 100 ns were carried out for each system (Mohammed Zaidh et al., 2025; Jayaraj and Hemalatha, 2024, Edwin et al., 2025).

RESULTS AND DISCUSSION

Analysis of Molecular Interactions with Silver Nitrate ($AgNO_3$)

The computational evaluation revealed a well-defined hierarchy in the adsorption behaviour of phytochemicals on $AgNO_3$ surfaces, with larger and more polar organic molecules exhibiting markedly stronger surface affinity.

Among the analysed compounds, Sitoindoside II showed the highest adsorption strength (−88.69 on the $AgNO_3$-6 surface), which can be attributed to its glycosidic framework enriched with multiple hydroxyl groups that support extensive hydrogen bonding and favourable van der Waals contacts with the $AgNO_3$ lattice. Similarly, 1,3,6-tri-O-galloyl-β-D-glucose displayed substantial adsorption energy (−51.40 on $AgNO_3$-7), driven by its galloyl moieties that provide multiple coordination points for Ag^+ ions, resulting in stable surface-associated complexes. Steroidal and terpenoid scaffolds also demonstrated notable adsorption behaviour. 4-Epicycloeucalenone (−55.97 on $AgNO_3$-7) maintained consistent surface association across multiple configurations, likely due to its rigid steroidal backbone combined with polar ketone functionality that enhances electrostatic complementarity with the metal surface. Pogostol exhibited appreciable adsorption (−45.40), where the presence of a hydroxyl group within a compact sesquiterpenoid framework promoted favourable surface contact and orientation. Sitoindoside IV (−66.98) showed adsorption behaviour comparable to that of Sitoindoside II, with slight differences in binding energy arising from variations in glycosidic linkages and molecular conformation. Collectively, the strongest adsorbates shared common molecular features, including high polar surface area, the presence of multiple functional groups capable of hydrogen bonding and metal coordination, and sufficient conformational adaptability to maximise surface contact.

In contrast, smaller and less functionalized molecules, such as 2-hexanone, displayed minimal adsorption, underscoring the importance of molecular size and interaction diversity in nano-interface stability. Consistent trends were also observed in electronic descriptors, where higher electronegativity values ($\chi > 50$) and negative mixing energies (E_mix) correlated with stronger adsorption, supporting their utility as predictive indicators of surface interaction efficiency.

Adsorption Locator Simulation Findings and Mechanistic Insights

Adsorption Locator simulations enabled detailed, atomistic characterization of the binding mechanisms underlying phytochemical interactions with $AgNO_3$ surfaces.

The strong adsorption observed for Sitoindoside II is closely associated with its high cohesive energy (average E_ss = −17.80) and conformational adaptability, which allow the molecule to achieve extensive surface coverage while maintaining favourable orientation of hydroxyl groups for hydrogen-bond formation. In contrast, 1,3,6-tri-O-galloyl-β-D-glucose exhibited a distinct binding mode dominated by its galloyl units, which engage in coordination interactions with surface Ag^+ ions. These chelation-driven contacts contribute to the formation of particularly stable surface complexes that are resistant to displacement. The adsorption behaviour of 4-epicycloeucalenone was governed by its rigid steroidal scaffold, which preferentially aligned parallel to the $AgNO_3$ surface. This orientation facilitates strong dipolar interactions between ketone oxygen atoms and surface silver cations, resulting in consistent adsorption across multiple surface configurations. For Pogostol, surface association was primarily mediated by its terminal hydroxyl group, which functions as both a hydrogen bond donor and acceptor, while the constrained bicyclic framework limited unfavourable conformational rearrangements upon adsorption. A notable outcome of the simulations was the identification of distinct adsorption geometries among different molecular classes.

Flexible glycosides, such as the Sitoindosides, adopted three-dimensional conformations that maximized multipoint surface interactions, whereas structurally rigid compounds, including 4-epicycloeucalenone, favoured flat-lying orientations that optimized electrostatic complementarity. In addition, surface heterogeneity played a significant role in adsorption strength, with step edges and kink sites on the $AgNO_3$ surface exhibiting substantially higher binding energies compared with ideal crystalline regions. A representative adsorption geometry of a phytochemical on the $AgNO_3$ surface, illustrating the preferred binding orientation and close contact with surface Ag^+ sites, is shown in Figure 1.

Collectively, these findings provide mechanistic insight into structure–adsorption relationships at the nano-interface. Strong, multipoint attachment observed for Sitoindoside II suggests potential utility in applications requiring stable surface functionalization, while the coordination-driven binding of tri-O-galloyl-β-D-glucose highlights its relevance for surface-mediated catalytic systems. The consistent adsorption behaviour of 4-epicycloeucalenone across surface environments further supports its suitability for applications where reproducible surface interactions are required. Overall, the quantitative structure–activity trends derived from these simulations offer a predictive framework for assessing the adsorption behaviour of structurally related compounds on $AgNO_3$ surfaces. The comparative adsorption energies and electronic descriptors for the top adsorbing phytochemicals are summarized in Table 1.

Table 1: Comparative of Top Adsorbing phytochemical on $AgNO_3$

Molecule	Method	Adsorption Energy (dEad, kcal/mol)	Chi (298 K)	Emix (298 K)	Ess avg (kcal/mol)	Key Binding Features
Sitoindoside II-muscapradisca	Blender	-88.69 ($AgNO_3$-6)	69.30	41.04	-17.80	Multi-point H-bonding, high e^- density
	Adsorption Locator	-67.68 ($AgNO_3$-1)	-	-	-16.38	Cohesive forces, surface deformation
tri-O-galloyl-beta-D-glucose	Blender	-51.40 ($AgNO_3$-7)	51.03	30.22	-13.31	Galloyl-Ag^+ coordination
	Adsorption Locator	-53.84 ($AgNO_3$-8)	-	-	-12.26	Multidentate chelation
4-Epicycloeucalenone-	Blender	-55.97 ($AgNO_3$-7)	42.99	25.46	-11.67	Steroid-ketone alignment
	Adsorption Locator	-48.46 ($AgNO_3$-1)	-	-	-10.99	Planar adsorption

Pogostol	Blender	-45.40 ($AgNO_3$-6)	15.71	9.30	-5.57	Rigid hydroxyl binding
	Adsorption Locator	-88.69 ($AgNO_3$-6)	-	-	-9.95	Terminal -OH interaction
Sitoindoside IV muscapradisica	Blender	-66.98 ($AgNO_3$-6)	62.22	36.85	-16.10	Glycosidic H-bonding
	Adsorption Locator	-61.25 ($AgNO_3$-9)	-	-	-15.40	Surface defect stabilization

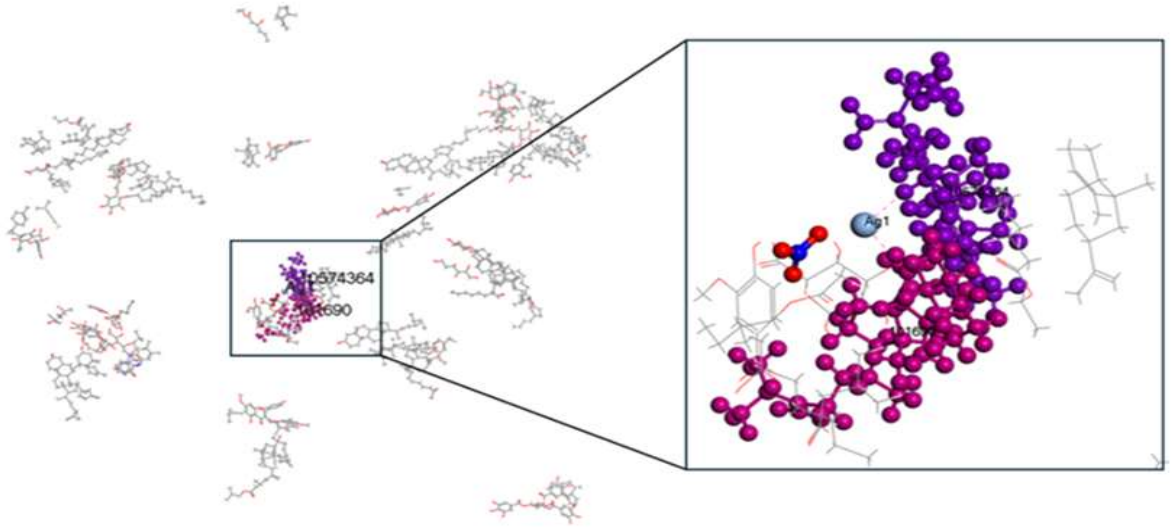

Figure 1. Interaction of a representative phytochemical with the $AgNO_3$ surface on the magnified view shows the preferred binding orientation and close contact with surface Ag^+ sites, highlighting stabilizing intermolecular interactions at the nano-interface.

Protein Preparation and Grid generation

Preparation and evaluation of the target proteins were carried out to ensure structural integrity and suitability for ligand interaction studies. The PPARγ structure (PDB ID: 7AWC), shown in Figure 2 a and b, was refined through correction of bond orders, addition of hydrogen atoms, and optimization of protonation states under physiological conditions. Energy minimization removed unfavourable contacts while maintaining the native α-helical framework of the receptor. The co-crystallized ligand was used to define the binding site and was removed during grid generation to preserve the native interaction environment of the cavity. The resulting structure retained a well-defined and compact ligand-binding pocket, suitable for evaluating small-molecule interactions.

The insulin receptor ectodomain (PDB ID: 7BW8), shown in Figure 2c and d, underwent extensive preparation due to its large, multidomain nature. Structural refinement improved interdomain stability and corrected side-chain orientations critical for maintaining native fold and surface electrostatics. Because no small-molecule ligand was present, binding-site identification was performed computationally. SiteMap analysis revealed a cavity with a D score exceeding 1.0, indicating a druggable organic binding site with favourable enclosure, hydrophobic balance, and hydrogen-bonding potential.

This high-scoring pocket was selected for grid generation and downstream docking studies. Together, these results confirm that both 7AWC and 7BW8 possess structurally stable and chemically suitable binding environments, supporting their use in systematic evaluation of phytochemical interactions.

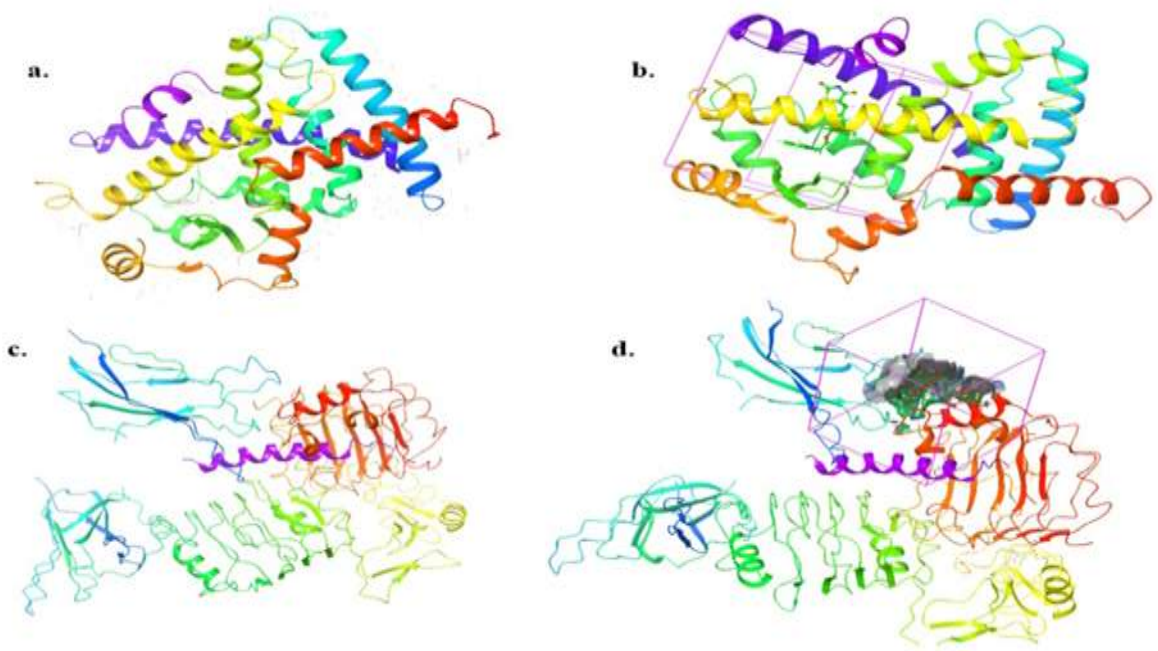

Figure 2. (a) Prepared structure of PPARγ (PDB ID: 7AWC), (b) Ligand-binding cavity and grid generation, (c) Prepared structure of the human insulin receptor ectodomain (PDB ID: 7BW8), and (d) Illustrating its multidomain organization and the computationally identified organic binding pocket (Dscore > 1.0) selected for docking and molecular dynamics simulations.

Molecular Docking

Molecular docking against PPARG (PDB ID: 7AWC) revealed that the selected fruit-derived phytochemicals bind stably within the canonical ligand-binding domain, forming interaction networks comparable to or stronger than the standard drug acarbose. Among the tested compounds, syringin (banana) exhibited the most favourable docking score (−8.366 kcal/mol) and a markedly low MM-GBSA binding free energy (−64.01 kcal/mol), (Table 2) indicating strong thermodynamic stabilization within the PPARG pocket. In Figure 3b Syringin established multiple hydrogen bonds with Ser289, His323, His449, and Tyr473, residues known to be critical for PPARG activation, along with hydrophobic contacts involving Leu330, Ile341, and Met364, which contributed to anchoring the ligand within the lipophilic region of the cavity.

In Figure 3a 1,3,6-tri-O-galloyl-β-D-glucose (mango) showed moderate docking affinity (−6.188 kcal/mol) but demonstrated a well-organized hydrogen-bonding network through its multiple hydroxyl groups, interacting with Glu343, Arg288, Ser342, and Tyr327, suggesting that polar contacts play a dominant role in its binding mode. In Figure 3c β-Bisabolene (mango), despite a relatively weaker docking score (−5.768 kcal/mol), displayed favourable MM-GBSA energy (−51.40 kcal/mol), driven largely by hydrophobic interactions with Leu255, Val339, Ile262, and Met348, highlighting the contribution of nonpolar stabilization within the PPARG cavity.

In Figure 3d Isopentyl benzoate (jackfruit) also maintained stable binding through π–alkyl and hydrophobic interactions with Phe363, Leu330, Ile341, and Met364, supported by a single hydrogen bond with Ser289, resulting in a balanced docking and MM-GBSA profile.

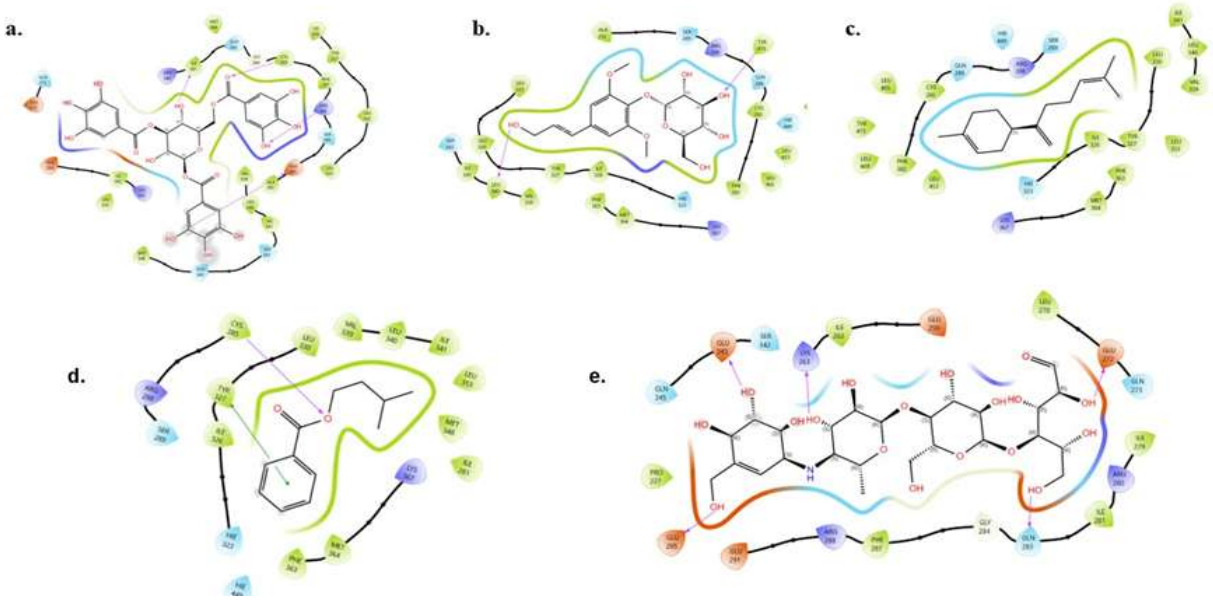

Figure 3. Two-dimensional interaction diagrams illustrating ligand binding within the PPARG active site (PDB ID: 7AWC): (a) 1,3,6-tri-O-galloyl-β-D-glucose (mango) showing extensive hydrogen bonding and π–π interactions, (b) syringin (banana) highlighting mixed polar and hydrophobic contacts, (c) β-bisabolene (mango) dominated by hydrophobic and π–alkyl interactions, (d) isopentyl benzoate (jackfruit) exhibiting ester moiety–driven hydrophobic stabilization, and (e) acarbose (standard drug) displaying multiple hydroxyl-mediated hydrogen bonds that anchor the ligand within the binding pocket.

Table 2: Docking scores and MM-GBSA binding free energy estimates of selected fruit-derived top 5 phytochemicals and acarbose within the PPARγ ligand-binding domain (PDB ID: 7AWC)

S. No	Compound (Source)	Docking Score (kcal/mol)	MM-GBSA ΔG (kcal/mol)
A	1,3,6-tri-O-galloyl-β-D-glucose (Mango)	−6.188	−29.22
B	Syringin (Banana)	−8.366	−64.01
C	β-Bisabolene (Mango)	−5.768	−51.40
D	Isopentyl benzoate (Jackfruit)	−6.336	−43.25
E	Acarbose (Standard drug)	−5.615	−26.28

The standard drug acarbose (Figure 3e) demonstrated comparatively weaker docking (−5.615 kcal/mol) and MM-GBSA energy (−26.28 kcal/mol); however, its interaction pattern was highly specific and biologically relevant. Acarbose formed persistent hydrogen bonds with Glu343, Arg288, Ser342, Tyr327, and His323, along with water-mediated contacts involving Gln286 and Lys367, reflecting its known polar binding mechanism.

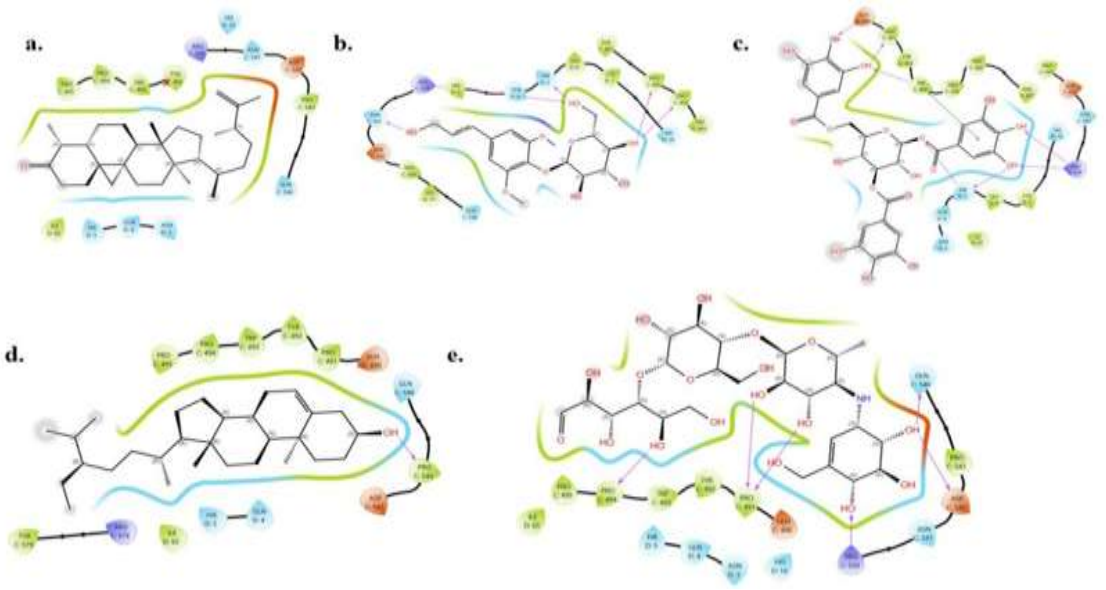

Figure 4. Interaction maps of ligands within the insulin receptor binding cavity (PDB ID: 7BW8): (a) 4-epicyclomusalenone (banana) showing hydrophobic and alkyl-driven stabilization, (b) syringin (banana) illustrating combined glycosidic hydroxyl hydrogen bonding and aromatic π–alkyl interactions, (c) 1,3,6-tri-O-galloyl-β-D-glucose (mango) highlighting extensive phenolic and sugar-moiety-mediated hydrogen bonding, and (d) acarbose (standard drug) displaying a dense network of hydroxyl-driven polar interactions anchoring the ligand within the organic binding cavity.

Interaction mapping revealed that ligand recognition by the insulin receptor (PDB ID: 7BW8) is strongly governed by the chemical moieties presented by each compound rather than by overall molecular size alone. In Figure 4a polyhydroxylated ligands such as 1,3,6-tri-O-galloyl-β-D-glucose, the galloyl phenolic rings and glucose core hydroxyl groups played a dominant role in binding. The phenolic –OH groups formed persistent hydrogen bonds with Glu542, Asp535, and Gln541, while the aromatic galloyl moieties established π-associated contacts with nearby aliphatic residues, enhancing both directional anchoring and surface complementarity (Bharathy et al., 2025; Srinivasan et al., 2025).

This dual polar–aromatic interaction pattern contributed to the deep embedding of the ligand within the organic cavity and accounted for its highly favourable binding free energy. The docking scores and MM-GBSA binding free energies for these ligands within the insulin receptor binding region are listed in Table 3.

Table 3: Molecular docking scores and MM-GBSA binding free energy estimates for selected fruit-derived phytochemicals and the reference drug acarbose interacting with the insulin receptor binding region (PDB ID: 7BW8).

S. No	Molecule name	Docking Score (kcal/mol)	MM-GBSA (kcal/mol)
a	4-Epicyclomusalenone (banana, $AgNO_3$-associated)	−3.927	−42.58
b	Syringin (banana)	−6.178	−49.00
c	1,3,6-tri-O-galloyl-β-D-glucose (mango)	−6.407	−56.90
d	β-Sitosterol (jackfruit)	−3.805	−38.66

e	Acarbose (standard drug)	−4.188	−44.82

For syringin, (Figure 4b) interaction stability was driven by the cooperative contribution of its phenylpropanoid aromatic ring and glycosidic hydroxyl groups. The aromatic ring aligned along a hydrophobic groove formed by Leu570, Val574, and Ile585, producing π–alkyl interactions, whereas the sugar hydroxyls interacted with Asn546 and His710 through hydrogen bonding. This balanced distribution of polar and nonpolar contacts enabled syringin to maintain conformational stability without excessive steric restriction. In contrast, β-sitosterol and 4-epicyclomusalenone relied primarily on their steroidal and sesquiterpene hydrocarbon frameworks, respectively.
These bulky hydrophobic moieties occupied the nonpolar core of the cavity and interacted predominantly with Pro495, Pro543, and Val574 via alkyl–alkyl contacts, with minimal involvement of polar residues. The reference drug acarbose displayed an interaction pattern primarily driven by its oligosaccharide scaffold, forming a dense hydrogen-bonding network with residues Glu542, Asp535, Gln541, and Asn546. Illustrated in Figure 4 c and d This resulted in strong electrostatic stabilization but limited hydrophobic engagement, leading to moderate cavity filling compared to aromatic phytochemicals.

MD Simulation

The backbone RMSD profiles show clear differences in stability for the 7AWC complexes formed with acarbose and 1,3,6-tri-O-galloyl-β-D-glucose In the acarbose-bound system (Figure. 5a), the protein RMSD increased from about 1.8 Å to around 2.6–2.8 Å during the first 30 ns before levelling off. This indicates a gradual structural adjustment of the PPARG binding domain. The ligand RMSD had marked spikes over 4.5 Å in the early phase, reflecting significant internal flexibility and frequent repositioning of the acarbose molecule in the binding pocket. Although the ligand RMSD later stabilized near 1.0–1.2 Å, these early fluctuations suggest weaker initial anchoring and dependence on flexible polar contacts rather than rigid stabilization. the 1,3,6-tri-O-galloyl-β-D-glucose -bound complex (Figure. 5b) showed stronger interaction stability and tighter control over its shape. The protein RMSD quickly settled and stayed between 2.2–2.6 Å throughout the 100 ns simulation, indicating minimal disturbance of the PPARG backbone. Notably, the ligand RMSD for 1,3,6-tri-O-galloyl-β-D-glucose mostly remained below 2.0 Å, with only slight changes, showing that the ligand kept a stable position inside the binding cavity.
This lower RMSD variation indicates strong anchoring interactions, thanks to the rigid galloyl aromatic rings and several directional hydrogen bonds that effectively secure the ligand. Analysis of residue-level flexibility supported these conclusions.

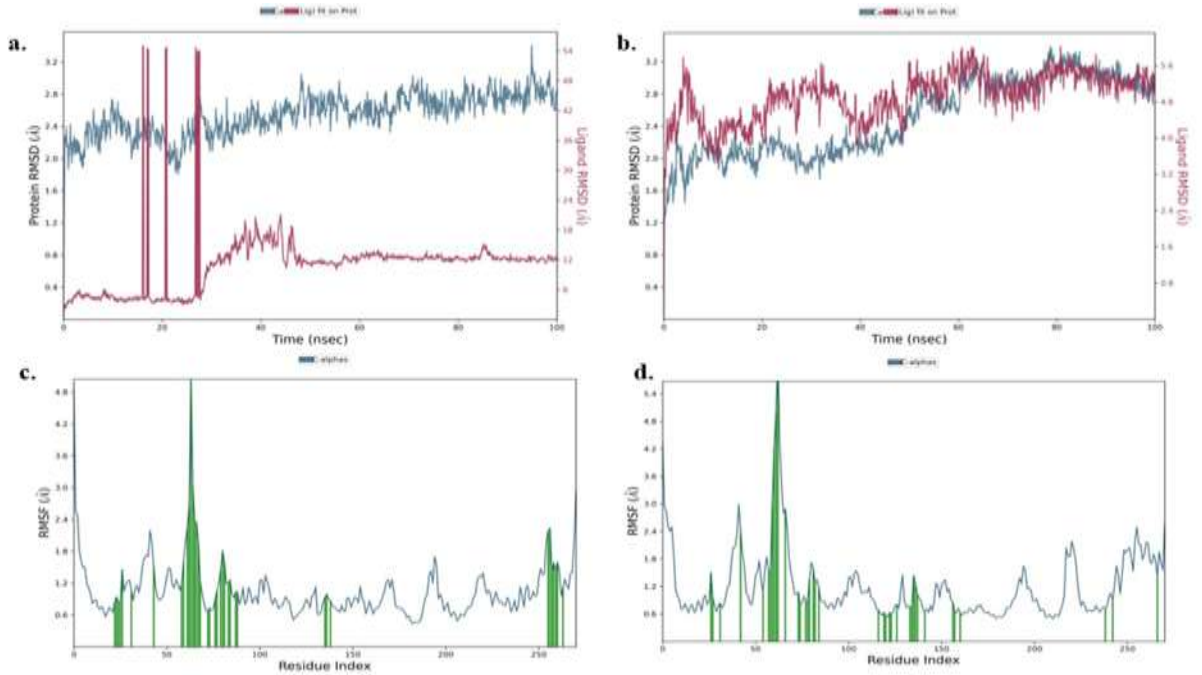

Figure 5. MD stability analysis of 7AWC complexes over a 100 ns simulation: (a) Time evolution of protein backbone RMSD and ligand RMSD for the acarbose–7AWC complex, (b) Corresponding RMSD profiles for the 1,3,6-tri-O-galloyl-β-D-glucose (TRI)–7AWC complex, (c) Residue-wise RMSF distribution of 7AWC in the presence of acarbose, and (d) RMSF profile of 7AWC bound to 1,3,6-tri-O-galloyl-β-D-glucose, highlighting reduced residue fluctuations and enhanced structural stabilization.

In the acarbose–PPARγ complex (Figure 5c), several loop regions and residues adjacent to the binding pocket exhibited elevated RMSF values ranging from 3.5 to 4.8 Å, particularly near the ligand entry region and solvent-exposed surfaces. This behaviour indicates localized flexibility associated with ligand rearrangement during the simulation.

In contrast, the TRI-bound system (Figure 5d) showed markedly reduced residue fluctuations, with most binding-site residues remaining below 2.0 Å. Increased mobility was limited to a small number of peripheral residues, while the core cavity residues remained conformationally stable.

The observed suppression of residue-level motion highlights the stabilizing influence of 1,3,6-tri-O-galloyl-β-D-glucose on the PPARγ binding domain. Consistent with this trend, lower RMSD values, diminished RMSF peaks, and rapid equilibration in the TRI–7AWC complex collectively indicate enhanced binding stability and improved dynamic compatibility relative to the acarbose-bound system.

The interaction fraction analysis (Figure 6a) illustrates the residue-specific engagement of acarbose within the PPARγ binding pocket over the 100 ns molecular dynamics simulation. Acarbose exhibited frequent and persistent interactions with several polar and charged residues lining the cavity, indicating stable binding primarily mediated by hydrogen bonding. Residues including Glu289, Ser289, His323, Tyr327, Glu343, Arg288, and Ser342 showed high interaction fractions, reflecting their consistent contribution to ligand stabilization. The stacked interaction profile demonstrates that hydrogen bonds were the predominant interaction type, with additional contributions from water-mediated bridges and occasional electrostatic contacts, highlighting the role of solvent-assisted stabilization. The interaction pattern is consistent with the chemical features of acarbose (Figure 6b), which contains multiple vicinal hydroxyl groups and glycosidic linkages capable of forming extensive hydrogen-bond networks. These functional groups repeatedly interacted with polar side chains and backbone atoms within the binding site, enabling sustained cavity engagement despite the molecule's conformational flexibility.

However, the relative absence of aromatic or hydrophobic regions limited persistent van der Waals anchoring, resulting in a binding mode that remained dynamically stable but less rigidly constrained within the pocket.

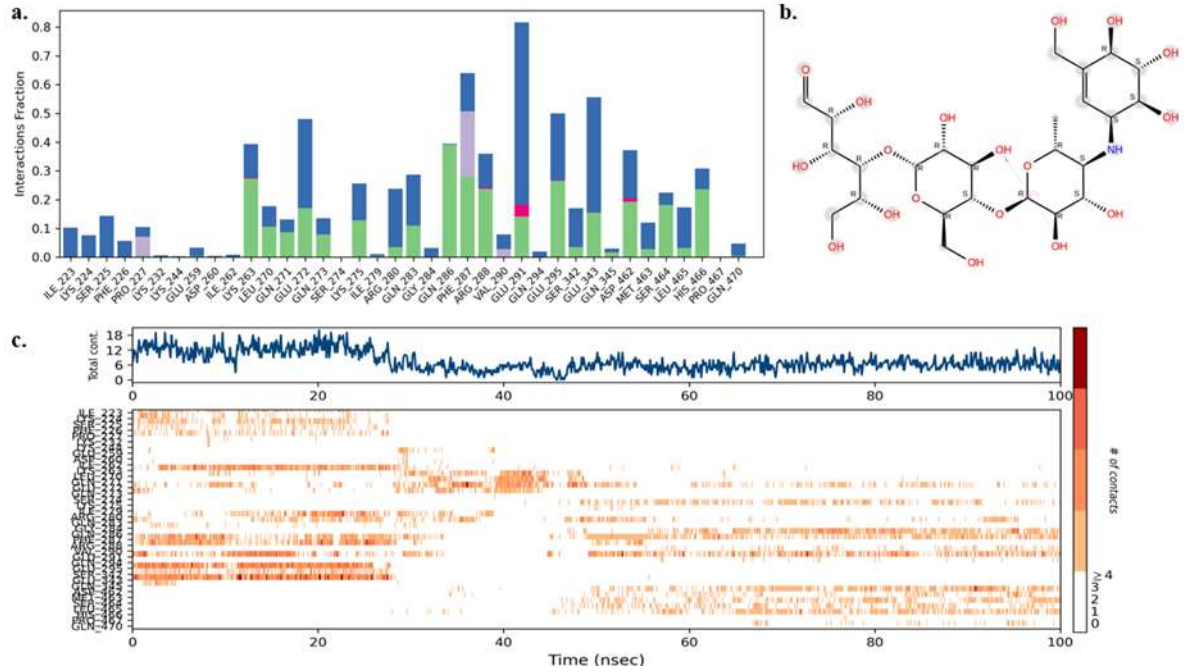

Figure 6. Interaction fraction and contact analysis of acarbose bound to PPARγ (7AWC) (a) Residue-wise interaction fraction highlighting dominant hydrogen-bond contributions (b) Chemical structure of acarbose

illustrating functional groups involved in receptor binding. (c) Time-resolved contact map and total interaction profile showing persistent ligand–residue contacts over the 100 ns simulation.

Time-resolved contact analysis showed that acarbose maintained continuous interactions with a defined group of residues within the 7AWC binding pocket, even as the ligand underwent conformational adjustments during the simulation. Among these, Glu289 and Glu343 emerged as the most persistent interaction partners, forming long-lived hydrogen bonds with multiple hydroxyl groups of acarbose throughout most of the 100 ns trajectory.

These acidic residues functioned as primary anchoring sites, preserving ligand association through repeated donor–acceptor interactions that remained largely intact during ligand reorientation events.

Additional stabilization was provided by Ser289, Ser342, and Tyr327, which exhibited frequent yet moderately dynamic contacts. The hydroxyl groups of serine residues supported short-range hydrogen bonding, whereas Tyr327 contributed through a combination of hydrogen bonding and polar–π interactions with the carbohydrate rings. His323 showed intermittent but recurring contacts, particularly during the mid and late stages of the simulation, suggesting a supportive role in maintaining ligand orientation rather than acting as a dominant anchor. Arg288 contributed sporadically through electrostatic and hydrogen-bond interactions, often facilitated by interfacial water molecules. Collectively, this interaction pattern indicates that acarbose binding is stabilized by a core set of polar residues (Glu289, Glu343, Ser289, and Ser342), with auxiliary contributions from His323, Tyr327, and Arg288 that adaptively reinforce ligand positioning (Figure 6c). analysis of the TRI–7AWC interaction profile (Figure 7a) revealed a broader and more persistent interaction network within the PPARγ binding cleft. Unlike the flexible carbohydrate ligands, TRI displayed consistently high interaction fractions with multiple residues over the entire 100 ns simulation. Key residues—including Glu289, Arg288, His323, Tyr327, Glu343, and Ser342—played dominant roles in stabilizing TRI, primarily through sustained hydrogen bonding. Stacked interaction bar plots further indicated notable contributions from π–π stacking and hydrophobic interactions, highlighting the dual polar–aromatic nature of TRI–receptor associations.

The two-dimensional interaction map of TRI (Figure 7b) underscores its distinctive binding architecture.

The three galloyl phenyl rings of TRI acted as rigid anchoring units, occupying hydrophobic sub-pockets formed by residues such as Leu330, Ile341, Met364, and Phe363, where π-alkyl and π–π interactions were observed. Concurrently, the glucose core and phenolic hydroxyl groups formed hydrogen bonds with acidic and polar residues, including Glu289, Glu343, Ser289, and Asn329.

The presence of these complementary interaction planes - distributed across both hydrophobic and polar regions—resulted in enhanced positional stability and limited excessive ligand movement, thereby restricting conformational freedom and reinforcing TRI retention within the PPARγ binding cavity.

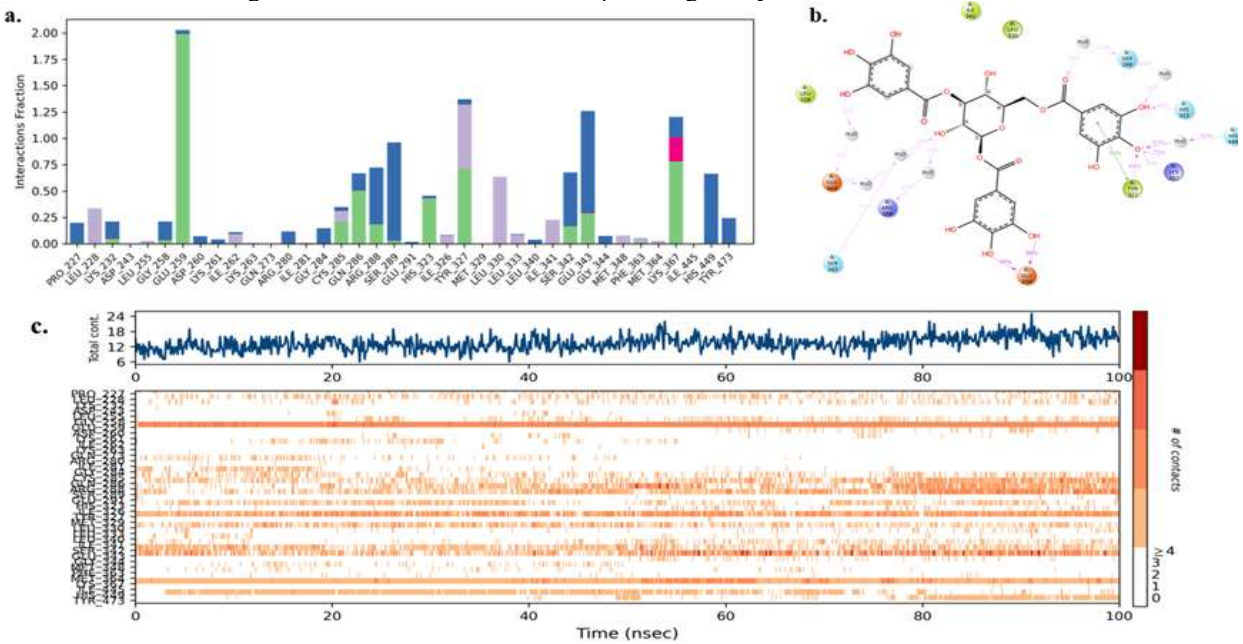

Figure 7. Interaction analysis of 1,3,6-tri-O-galloyl-β-D-glucose bound to PPARγ (7AWC).
(a) Residue-wise interaction fraction illustrating sustained hydrogen-bonding and aromatic interactions, (b) Two-dimensional ligand–residue interaction map highlighting the contribution of galloyl moieties and glucose

hydroxyl groups, and (c) Time-resolved contact profile demonstrating persistent and well-distributed interactions throughout the simulation.

Time-resolved contact mapping demonstrated that 1,3,6-tri-O-galloyl-β-D-glucose (TRI) forms a highly persistent and well-distributed interaction network within the PPARγ binding domain (PDB ID: 7AWC) throughout the 100 ns molecular dynamics simulation.

Among the most consistently involved residues, Glu289 and Glu343 exhibited near-continuous contacts, establishing stable hydrogen bonds with both phenolic and glycosidic hydroxyl groups of TRI.

These acidic residues functioned as principal anchoring sites, restricting ligand displacement and contributing substantially to long-term complex stability. Ser289 and Ser342 further reinforced this network through frequent hydrogen-bond interactions, enabling fine positional adjustments of the ligand without disrupting the overall binding geometry. Aromatic and semi-polar residues contributed additional stabilization. Tyr327 maintained recurring contacts across the trajectory, participating in hydrogen bonding and π-associated interactions with the galloyl rings, thereby supporting aromatic stacking and orientation control. His323 displayed intermittent yet reproducible interactions, particularly during the middle and later stages of the simulation, suggesting a role in preserving ligand alignment rather than acting as a fixed anchor. Arg288 formed occasional electrostatic and hydrogen-bond interactions, some mediated by interfacial water molecules, which aided stabilization of the negatively polarized galloyl groups during conformational adjustments. Hydrophobic residues lining the interior of the binding pocket, including Leu330, Ile341, Met364, and Phe363, contributed repeated van der Waals contacts with the aromatic moieties of TRI, generating a nonpolar environment that further reduced ligand mobility. The persistence of these interactions, together with sustained polar anchoring by Glu- and Ser-rich regions, resulted in consistently high contact frequencies with minimal long-term disruption.

Overall, the time-resolved analysis indicates that TRI binding to 7AWC is governed by a cooperative and durable interaction network involving acidic, polar, aromatic, and hydrophobic residues, collectively ensuring strong and dynamically stable receptor engagement.

Distinct differences in dynamic behaviour were observed for the insulin receptor ectodomain (7BW8) when bound to acarbose and 4-epicyclomusalenone. In the acarbose-bound system (Figure 8a), the protein backbone RMSD increased gradually from approximately 3.5 Å to around 5.5–6.0 Å over the 100 ns simulation, reflecting progressive conformational adaptation. The ligand RMSD showed a steady rise accompanied by pronounced fluctuations, exceeding 15 Å during the later stages of the trajectory. This behaviour suggests substantial internal rearrangement and positional shifting of acarbose within the binding region, consistent with its flexible, hydroxyl-rich oligosaccharide structure and dependence on transient polar interactions rather than rigid anchoring. The 4-epicyclomusalenone–7BW8 complex (Figure 8b) displayed a more stabilized RMSD profile following initial equilibration. The protein backbone RMSD increased during the early phase and subsequently fluctuated within a narrower range of approximately 4.5–5.8 Å, indicating attainment of a dynamically stable conformational state. Ligand RMSD values for 4-epicyclomusalenone remained consistently lower and exhibited fewer large excursions compared with acarbose, reflecting reduced ligand mobility within the binding cavity. This enhanced stability is attributable to the compact and hydrophobic sesquiterpene scaffold, which favours sustained van der Waals and alkyl interactions with nonpolar receptor residues. Residue-level flexibility analysis further supported these observations. The RMSF profile of the acarbose-bound complex (Figure 8c) showed pronounced fluctuations in several loop regions and solvent-exposed segments, with RMSF values exceeding 6–8 Å for specific residues, indicating localized structural plasticity likely driven by repeated ligand repositioning and solvent-mediated interactions.

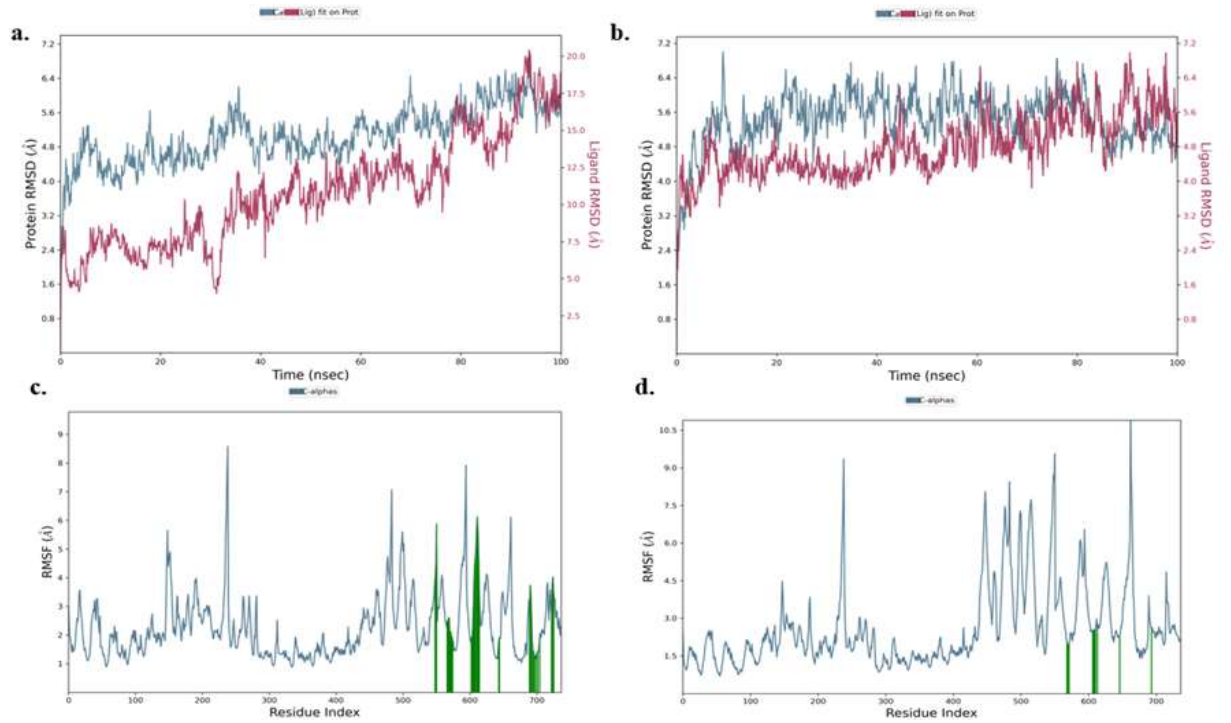

Figure 8. Molecular dynamics stability analysis of insulin receptor ectodomain (7BW8) complexes over a 100 ns simulation (a) Protein backbone RMSD and ligand RMSD for the acarbose–7BW8 complex, (b) Corresponding RMSD profiles for the 4-epicyclomusalenone–7BW8 complex, (c) Residue-wise RMSF distribution for the acarbose-bound system, and (d) RMSF profile of the 4-epicyclomusalenone-bound system indicating comparatively reduced residue fluctuations.

The RMSF profile of the 4-epicyclomusalenone–7BW8 complex (Figure 8d) displayed lower fluctuation amplitudes across most residues, with the majority remaining below 4 Å. Although flexibility persisted in a few distal loop regions, residues directly involved in ligand interaction exhibited restricted motion, indicating enhanced local stabilization. Taken together, the RMSD and RMSF analyses demonstrate that 4-epicyclomusalenone imparts greater dynamic stability to the 7BW8 protein than acarbose, despite forming fewer polar contacts.

While acarbose relies on extensive hydrogen bonding for receptor engagement, its high conformational flexibility results in increased ligand mobility and elevated protein fluctuations.

In contrast, the compact and hydrophobic scaffold of 4-epicyclomusalenone supports sustained cavity occupation, limits ligand displacement, and promotes stabilization of the receptor architecture. These observations highlight the importance of hydrophobic anchoring and structural rigidity in maintaining long-term stability of insulin receptor–ligand complexes. The interaction fraction analysis for the acarbose–7BW8 complex (Figure 9a) revealed persistent and multivalent interactions with several residues within the binding pocket. Notably, Asp357, Asp361, Glu411, His592, and Asn594 showed high interaction, predominantly through hydrogen bonding. Among these, Asp357 and Glu411 exhibited the largest cumulative interaction fractions (>1.0), indicating the formation of multiple concurrent hydrogen bonds with distinct hydroxyl groups of acarbose. Additional contributions arose from Ser358, Thr360, and Gln595, which formed intermittent polar contacts that further supported ligand retention within the binding region. The two-dimensional interaction map (Figure 9b) provides molecular-level insight into these interactions, showing direct hydrogen-bond formation between the terminal hydroxyl and glycosidic oxygen atoms of acarbose and residues such as Asp357, His592, and Asn594. The central sugar ring was further stabilized through contacts with Glu411 and Ser358, while water-mediated bridges involving Thr360 and Gln595 contributed to interaction continuity during ligand rearrangement. This distributed interaction network enabled acarbose to remain associated with the binding pocket despite its inherent flexibility, anchoring the ligand across multiple regions of the receptor.

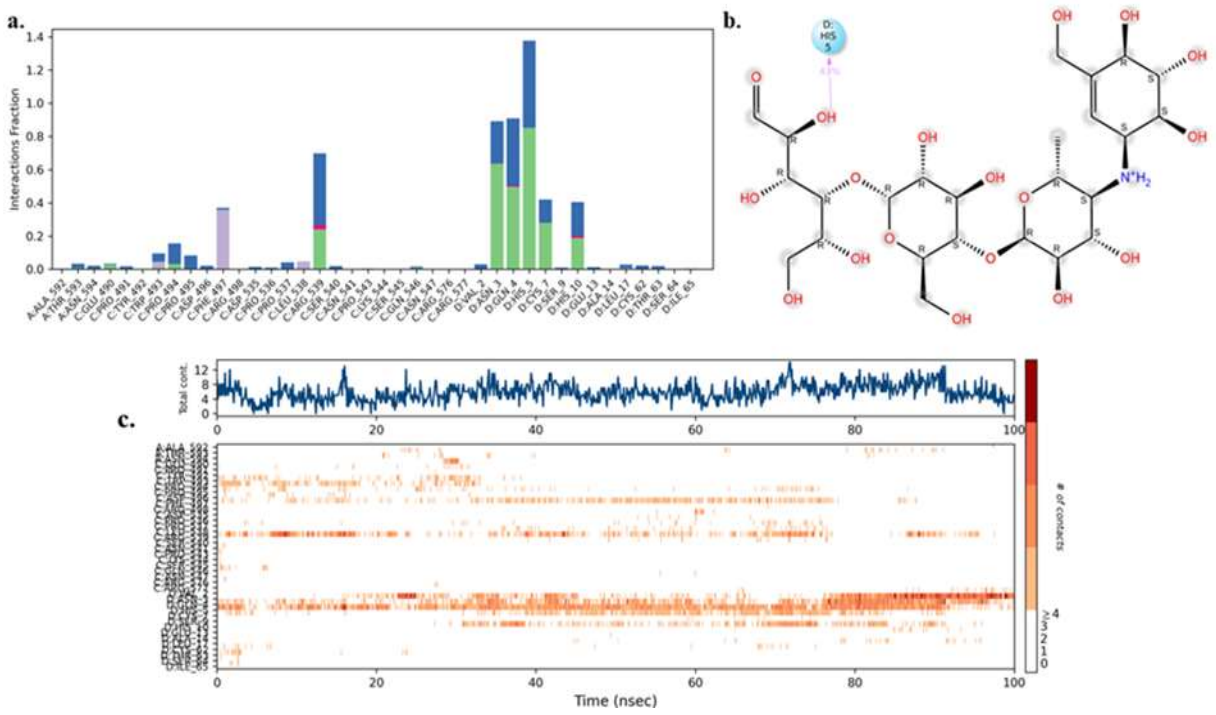

Figure 9. Interaction analysis of acarbose bound to the insulin receptor ectodomain (7BW8). (a) Residue-wise interaction fraction highlighting dominant hydrogen-bond interactions with acidic and polar residues, (b) Two-dimensional ligand–residue interaction map illustrating hydrogen-bonding and water-mediated contacts, and (c) Time-resolved contact map and total interaction profile demonstrating sustained ligand engagement over the simulation period.

The time-resolved contact map and total contact profile (Figure 9c) demonstrate the sustained stability of the acarbose–7BW8 complex throughout the 100 ns molecular dynamics simulation. Persistent interactions were maintained by key residues including Asp357, Asp361, Glu411, His592, and Asn594, each displaying continuous contact bands over the simulation timeline. The overall contact count remained consistently high with only minor fluctuations, indicating stable ligand retention and the absence of dissociation events. In particular, His592 and Asp357 showed uninterrupted interaction persistence, underscoring their central role in anchoring acarbose within the binding cavity.

Collectively, acarbose binding to 7BW8 is stabilized by a dense hydrogen-bonding network involving Asp357, Asp361, Glu411, His592, Asn594, and Gln595, further reinforced by auxiliary polar and solvent-mediated interactions. This cooperative interaction framework accounts for the strong binding stability observed during the simulation and highlights the importance of acidic and polar residues in accommodating carbohydrate-based inhibitors within the 7BW8 active site. The interaction fraction analysis for the 4-epicyclomusalenone–7BW8 complex (Figure 10a) reveals a more localized interaction pattern centered on a limited set of residues within the active cavity. Asn541 emerged as the principal interaction partner, exhibiting the highest contact persistence (≈0.85), consistent with a stable and long-lived hydrogen bond throughout the simulation. Ser540 provided secondary stabilization, showing a moderate interaction fraction (≈0.40) indicative of a supportive anchoring role. In addition to polar contacts, recurrent hydrophobic interactions were observed with Trp493 (≈0.45) and Tyr492 (≈0.18), where aromatic side chains contributed nonpolar and π-associated interactions with the rigid polycyclic scaffold of 4-epicyclomusalenone. Other residues, including Pro495, Pro543, Gln546, and Tyr579, displayed intermittent contacts, suggesting a role in maintaining binding pocket shape and spatial complementarity rather than serving as primary anchoring points

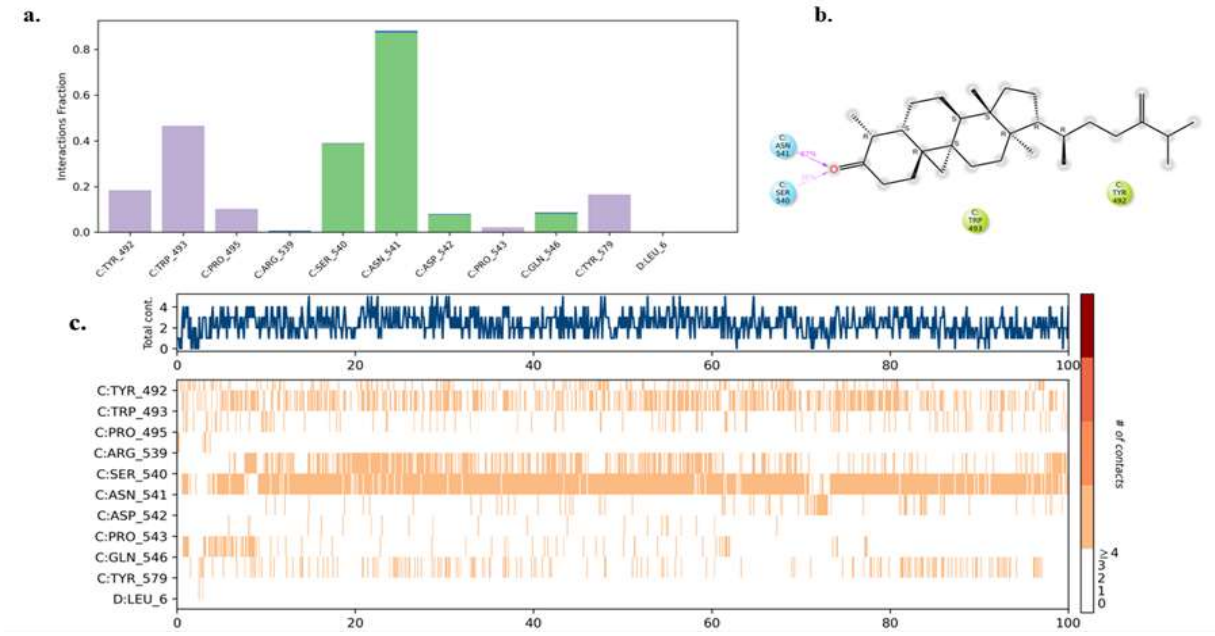

Figure 10. Interaction analysis of 4-epicyclomusalenone bound to 7BW8 (a) interaction fraction of key binding-site residues, (b) two-dimensional ligand–residue interaction map highlighting hydrogen-bond and hydrophobic contacts, and (c) total contact profile and residue-wise contact persistence over the 100 ns molecular dynamics simulation.

The ligand–residue interaction map (Figure 10b) clarifies the molecular basis of 4-epicyclomusalenone binding within the 7BW8 active site. The ligand's carbonyl and hydroxyl groups form stable hydrogen bonds predominantly with Asn541 and Ser540, providing the primary polar anchoring interactions. In parallel, the rigid steroid-like scaffold of 4-epicyclomusalenone fits into a hydrophobic pocket defined by Trp493 and Tyr492, where close packing is maintained through van der Waals and aromatic stacking interactions. These nonpolar contacts restrict excessive ligand movement and support a well-defined binding orientation. Time-resolved contact mapping and total interaction profiling (Figure 10c) show that the complex consistently maintains an average of three to four residue contacts across the 100 ns simulation, with minimal temporal fluctuation.

Continuous contact signatures for Asn541 and Ser540 confirm their dominant role in stabilizing the complex, while short-lived interactions with neighbouring residues reflect localized conformational adjustments rather than binding disruption. Overall, 4-epicyclomusalenone achieves stable accommodation within the 7BW8 binding cavity through the combined effects of persistent hydrogen bonding and hydrophobic enclosure, yielding a protein–ligand complex that is both structurally stable and dynamically resilient.

CONCLUSION

This study presents an integrated computational investigation of fruit-derived phytochemicals within a nano-assisted framework to evaluate their potential roles in regulating insulin signalling through two mechanistically interconnected targets: the insulin receptor ectodomain and peroxisome proliferator-activated receptor gamma (PPARγ). By combining molecular docking, binding free-energy calculations, nano-interface adsorption analysis, and extended molecular dynamics simulations, the work provides a multilayered view of ligand behaviour spanning static binding, interfacial stabilization, and dynamic conformational persistence. The findings demonstrate that several phytochemicals exhibit stable and energetically favourable interactions with both protein targets, supporting their capacity to engage distinct regulatory nodes of insulin signalling. Polyphenolic compounds displayed extensive hydrogen-bonding networks and aromatic interactions that promoted strong anchoring within the PPARγ binding cavity, while terpenoid-based molecules showed compact and hydrophobically driven binding profiles that enhanced stabilization of the insulin receptor domain. In contrast to the reference drug acarbose, which relied predominantly on flexible polar interactions, the identified phytochemicals achieved improved dynamic stability through a balanced combination of polar, aromatic, and nonpolar contacts.

The incorporation of $AgNO_3$-based nano-interface analysis further clarified the contribution of surface-mediated stabilization, revealing that molecular size, functional group density, and electronic properties collectively influence

adsorption strength and interfacial compatibility. These results suggest that nano-stabilization may play a supportive role in enhancing ligand retention and structural resilience, potentially addressing limitations related to phytochemical instability and inconsistent target engagement. Overall, this work highlights the utility of nano-enabled computational strategies for systematically identifying and characterizing bioactive dietary compounds with multi-target potential. By adopting a dual-target perspective and integrating protein–ligand dynamics with nano-interface behaviour, the study advances mechanistic insight into phytochemical modulation of insulin signalling. The computational evidence presented here establishes a rational basis for subsequent experimental validation and supports the further development of fruit-derived phytochemicals as complementary or lead candidates for antidiabetic therapeutic design.

ACKNOWLEDGMENT
The author sincerely acknowledges the support and guidance provided by the faculty members of the Department of Pharmaceutical Chemistry, Saveetha College of Pharmacy (SIMATS) Chennai; during the preparation of this article manuscript.

CONFLICTS OF INTERESTS (IF ANY)
There are no conflicts of interest.

FUNDING
None declared

AUTHORS CONTRIBUTION
Data Analysis or Interpretation and Manuscript Drafting - Priya Modhugur Sathyanarayanan. Study Conception or Design and Critical Manuscript Revision - Magesh Mohan. Data Acquisition - Pavithra Bharathy, Swathi T, Jaisri J. R, Akshaya Varshini S, and Nashwa S. All the authors read
and approved the final manuscript.

ABBREVIATIONS
$AgNO_3$: Silver nitrate; Å: Ångström; COMPASS: Condensed-phase Optimized Molecular Potentials for Atomistic Simulation Studies; DFT: Density Functional Theory; $Dmol^3$: Density-functional-based molecular simulation package; dEad: Adsorption energy; dEad/dNi: Gradient of adsorption energy with respect to the number of interacting surface atoms; Emix: Mixing energy; Ess: Screen–screen interaction energy; GAFF: General Amber Force Field; Glide XP: Glide Extra Precision; IMMPAT: Indian Medicinal Plants, Phytochemistry and Therapeutics Database; kcal/mol: Kilocalories per mole; MD: Molecular Dynamics; MM-GBSA: Molecular Mechanics–Generalized Born Surface Area; MM-PBSA: Molecular Mechanics–Poisson–Boltzmann Surface Area; ns: Nanosecond; NPT: Constant Number of particles, Pressure, and Temperature ensemble; NVT: Constant Number of particles, Volume, and Temperature ensemble; OPLS4: Optimized Potentials for Liquid Simulations Force Field version 4; PDB: Protein Data Bank; PI3K: Phosphoinositide 3-Kinase; PPARγ: Peroxisome Proliferator-Activated Receptor Gamma; PPARG: Peroxisome Proliferator-Activated Receptor Gamma Gene; RESP: Restrained Electrostatic Potential; RMSD: Root Mean Square Deviation; RMSF: Root Mean Square Fluctuation; SiteMap Schrödinger: SiteMap Binding Site Prediction Module; SMILES: Simplified Molecular Input Line Entry System; SPC: Simple Point Charge (water model); UFF: Universal Force Field; χ: Electronegativity.

REFERENCES

1. Williams JLS, Walker RJ, Smalls BL, Campbell JA and Egede LE (2014). Effective interventions to improve medication adherence in type 2 diabetes: a systematic review. Diabetes Manag. 4: 29-42.
2. The Lancet (2023). Diabetes: a defining disease of the 21st century. Lancet 401: 2087.
3. Hossain MJ, Al-Mamun M and Islam MR (2024). Diabetes mellitus, the fastest growing global public health concern: early detection should be focused. Health Sci. Rep. 7: e2004.
4. Rossi MC, Nicolucci A, Ozzello A, Gentile S, Aglialoro A, Chiambretti A, Baccetti F, Gentile FM, Romeo F, Lucisano G, Giorda CB and Fornengo R (2019). Impact of severe and symptomatic hypoglycemia on quality of life and fear of hypoglycemia in type 1 and type 2 diabetes: results of the Hypos-1 observational study. Nutr. Metab. Cardiovasc. Dis. 29: 736-743.
5. Antar SA, Ashour NA, Sharaky M, Khattab M, Ashour NA, Zaid RT, Roh EJ, Elkamhawy A and Al-Karmalawy AA (2023). Diabetes mellitus: classification, mediators, and complications; a gate to identify potential targets for the development of new effective treatments. Biomed. Pharmacother. 168: 115734.
6. Poznyak A, Grechko AV, Poggio P, Myasoedova VA, Alfieri V and Orekhov AN (2020). The diabetes mellitus-atherosclerosis connection: the role of lipid and glucose metabolism and chronic inflammation. Int. J. Mol. Sci. 21: 1835.
7. Parvin N, Aslam M, Joo SW and Mandal TK (2025). Nano-phytomedicine: harnessing plant-derived phytochemicals in nanocarriers for targeted human health applications. Molecules 30: 3177.

8. Kumar A, Nirmal P, Kumar M, Jose A, Tomer V, Oz E, Proestos C, Zeng M, Elobeid T, Sneha V and Oz F (2023). Major phytochemicals: recent advances in health benefits and extraction method. Molecules 28: 887.
9. Simon GE, Stewart C, Yarborough BJ, Lynch F, Coleman KJ, Beck A, Operskalski BH, Penfold RB and Hunkeler EM (2018). Mortality rates after the first diagnosis of psychotic disorder in adolescents and young adults. JAMA Psychiatry 75: 254-260.
10. Omer AE, Hojjati-Firoozabadi A, Gigoyan S, Safavi-Naeini S and Shaker G (2022). Non-reciprocal whispering-gallery-mode resonator for sensitive blood glucose monitoring. IEEE Trans. Instrum. Meas. 71: 3154823.
11. Momozawa Y, Mni M, Nakamura K, Coppieters W, Almer S, Amininejad L, Cleynen I, Colombel JF, De Rijk P, Dewit O, Finkel Y, Gassull MA, Goossens D, Laukens D, Lémann M, Libioulle C, O'Morain C, Reenaers C, Rutgeerts P and Georges M (2011). Resequencing of positional candidates identifies low-frequency IL23R coding variants protecting against inflammatory bowel disease. Nat. Genet. 43: 43-47.
12. Imran M, Ghorat F, Ul-Haq I, Ur-Rehman H, Aslam F, Heydari M, Shariati MA, Okuskhanova E, Yessimbekov Z, Thiruvengadam M, Hashempur MH and Rebezov M (2020). Lycopene as a natural antioxidant used to prevent human health disorders. Antioxidants (Basel) 9: 706.
13. Sayago-Ayerdi S, García-Martínez DL, Ramírez-Castillo AC, Ramírez-Concepción HR and Viuda-Martos M (2021). Tropical fruits and their co-products as bioactive compounds and their health effects: a review. Foods 10: 1952.
14. Willems S, Gellrich L, Chaikuad A, Kluge S, Werz O, Heering J, Knapp S, Lorkowski S, Schubert-Zsilavecz M and Merk D (2021). Endogenous vitamin E metabolites mediate allosteric PPARγ activation with unprecedented co-regulatory interactions. Cell Chem. Biol. 28: 1489-1500.e8.
15. Yu D, Zhang X, Sun J, Li X, Wu Z, Han X, Fan C, Ma Y, Ouyang Q and Wang T (2021). Cryo-EM structure for the insulin binding region in the ectodomain of the full-length human insulin receptor in complex with one insulin. Protein Data Bank. PDB ID: 7BW8.
16. Mohanraj K, Karthikeyan BS, Vivek-Ananth RP, Bharath Chand RP, Aparna SR, Mangalapandi P and Samal A (2018). IMPPAT: a curated database of Indian medicinal plants, phytochemistry and therapeutics. Sci. Rep. 8: 4329.
17. Tran N, Pham B and Le L (2020). Bioactive compounds in anti-diabetic plants: from herbal medicine to modern drug discovery. Biology (Basel) 9: 252.
18. Ma CY, Geatches D, Hsiao YW, Kwokal A and Roberts KJ (2023). Role of molecular, crystal, and surface chemistry in directing the crystallization of entacapone polymorphs on the Au(111) template surface. Cryst. Growth Des. 23: 4522-4537.
19. Kwokal A, Čavužić D and Roberts KJ (2013). Surface adsorbed templates for directing the crystal growth of entacapone as monitored using process analytical techniques. Cryst. Growth Des. 13: 5324-5334.
20. Vianello R, Domene C and Mavri J (2016). The use of multiscale molecular simulations in understanding a relationship between the structure and function of biological systems of the brain: the application to monoamine oxidase enzymes. Front. Neurosci. 10: 327.
21. Mehmood A, Nazir H, Luo Y, Ahmad K, Urooj F and Wu Y (2025). Harnessing Artemisia argyi phytochemicals: a deep learning and molecular docking approach for targeting cancer and inflammation. Netw. Model. Anal. Health Inform. Bioinform. 14: 162.
22. Ahamed HN, Ismail Y, Navabshan I, Mohammed Zaidh S, Shanmugarajan TS, Jaleel I and Ansari LHT (2024). Investigating the toxicity of malachite green and copper sulfate in brine shrimp: in vivo and computational study. Toxicol. Rep. 13: 101811.
23. Mohammed Zaidh S, Aher KB, Bhavar GB, Irfan N, Ahmed HN and Ismail Y (2023). Genes adaptability and NOL6 protein inhibition studies of fabricated flavan-3-ols lead skeleton intended to treat breast carcinoma. Int. J. Biol. Macromol. 127661.
24. Irfan N, Vaithyanathan P, Anandaram H, Mohammed Zaidh S, Varshini SP and Puratchikody A (2023). Active and allosteric site binding MM-QM studies of methylidene tetracyclo derivative in PCSK9 protein intended to make a safe antilipidemic agent. J. Biomol. Struct. Dyn. (in press).
25. Priya RM, Mohammed Zaidh S, Navabshan I, Venkataraman S, Ahmed HN and Ismail Y (2024). Pharmacophore-based SAR analysis and synthetic route review of imidazole core analogues. Curr. Appl. Sci. Technol. e0261082.
26. Mohammed Zaidh S, Vengateswaran HT, Habeeb M, Aher KB, Bhavar GB, Irfan N and Chenchu Lakshmi KNV (2025). Network pharmacology and AI in cancer research uncovering biomarkers and therapeutic targets for RALGDS mutations. Sci. Rep. 15: 10938.

27. Jayaraj S and Hemalatha K (2024). Design, synthesis, and anticancer evaluation of novel N-[5-(1,3,4,5-tetrahydroxycyclohexyl)-1,3,4-thiadiazole-2-yl] benzamide analogues through integrated computational and experimental approaches. Future J. Pharm. Sci. 10: 149.
28. Edwin MA, Velmurugan R and Patel S (2025). In silico evaluation of Acalypha indica phytochemicals as potential antifungal agents targeting Saccharomyces cerevisiae lanosterol 14-alpha demethylase. Cell Biochem. Biophys. 83: 5197-5215.
29. Bharathy P, Thanikachalam PV, Moses AC and Balakrishnan DK (2025). Exploring the wound healing potential of Ixora coccinea and Rhododendron arboreum formulation: integrating experimental and computational approaches. J. Complement. Integr. Med. 22: 304-318.
30. Srinivasan M, Ismail Y, Irfan N and Mohammed Zaidh S (2025). Synergistic suppression of cell growth: Phenmiazine derivatives targeting p53 and MDM2 unveiled through hybrid computational method. Comput. Biol. Chem. 115: 108344.